Importance of gas heating in capacitively coupled radiofrequency plasma-assisted synthesis of carbon nanomaterials

Tanvi Nikhar^{1,5}□, Sankhadeep Basu^{2,3,5}□, Shota Abe⁴, Shurik Yatom⁴, Yevgeny Raitses⁴□, Rebecca Anthony^{2,3,*} and Sergey V Baryshev^{1,2,*}□

- Department of Electrical and Computer Engineering, Michigan State University, East Lansing, MI 48824, United States of America
- Department of Chemical Engineering and Material Science, Michigan State University, East Lansing, MI 48824, United States of America
- Department of Mechanical Engineering, Michigan State University, East Lansing, MI 48824, United States of America
- Discovery Plasma Science Department, Princeton Plasma Physics Laboratory, Princeton, NJ 08542, United States of America

E-mail: ranthony@msu.edu and serbar@msu.edu

Received 6 May 2024, revised 25 June 2024 Accepted for publication 9 August 2024 Published 30 August 2024



Abstract

In pursuit of diamond nanoparticles, a capacitively-coupled radio frequency flow-through plasma reactor was operated with methane-argon gas mixtures. Signatures of the final product obtained microscopically and spectroscopically indicated that the product was an amorphous form of graphite. This result was consistent irrespective of combinations of the macroscopic reactor settings. To explain the observed synthesis output, measurements of C₂ and gas properties were carried out by laser-induced fluorescence and optical emission spectroscopy. Strikingly, the results indicated a strong gas temperature gradient of 100K per mm from the center of the reactor to the wall. Based on additional plasma imaging, a model of hot constricted region (filamentation region) was then formulated. It illustrated that, while the hot constricted region was present, the bulk of the gas was not hot enough to facilitate diamond sp^3 formation: characterized by much lower reaction rates, when compared to sp^2 , sp^3 formation kinetics are expected to become exponentially slow. This result was further confirmed by experiments under identical conditions but with a H₂/CH₄ mixture, where no output material was detected: if graphitic sp^2 formation was expected as the main output material from the methane feedstock, atomic hydrogen would then be expected to etch it away in situ, such that the net production of that sp^2 -hybridized solid material is nearly a zero. Finally, the crucial importance of gas heating was corroborated by replacing RF with microwave source whereby facile sp^3 production was attained with H₂/CH₄ gas mixture.

These authors contributed equally to this work.

^{*} Authors to whom any correspondence should be addressed.



Original Content from this work may be used under the terms of the Creative Commons Attribution 4.0 licence. Any

further distribution of this work must maintain attribution to the author(s) and the title of the work, journal citation and DOI.

© 2024 The Author(s). Published by IOP Publishing Ltd

Keywords: low temperature plasma, nanodiamond, nanographite, constricted discharge, carbon dimer density, microwave reactor, flow-through reactor nanocrystals. If diamond cubic Si nanocrystals are

Low-temperature plasmas (LTP) have been an enabling

1. Introduction

technology and indispensable tool for the microelectronics and semiconductor industry [1]. The critical importance of LTP technologies keeps growing in the modern era of sub-10 nm node 3D integration, where UV lithography, etching, passivation and ultrathin film growth are the most critical steps of integrated circuits fabrication and integration. At the same time, LTP-based syntheses occupy a special place in semiconductor nanomaterial manufacturing which is important in photovoltaics and quantum information sciences [2, 3]. Among other types of LTP reactors, sub-atmospheric capacitively-coupled radio frequency (CCRF) continuous flow-through reactors gained a lot of attention and implementations since the early 2000's due to their simplicity, high production rates/material yields, simple means of material collection and post-synthesis treatment and integration (including 3D printing) [4–16]. By now, flowthrough CCRF LTP reactors succeeded in creating a profound list compound (oxide, sulfide, nitride, and phosphide) and elemental group IV semiconductors[3]. Todate, syntheses of group IV nanomaterial s have included well-established and vetted synthetic routes for Si, Ge, and SiGe nanocrystals [17–19], SiC, and graphite

Historically, microwave plasma-assisted chemical vapor deposition (CVD) is used to deposit diamonds in bulk thin film form where substrate surface kinetics governs the growth. Gas phase diamond nucleation and growth is a subject that was studied much less. In the 1970's, Deryagin and Fedoseev proposed the possibility of nucleating diamond in the gas phase inside a plasma [20]. Experimental work on gas-phase nucleation was conducted by Frenklach et al at Penn State using a low-pressure microwave plasma. Assynthesized materials hadtobetreated and purified before submicrondiamondcrystals could be retrieved thereby proving Deryagin's hypothesis [21]. At that time, there were a limited number of reports corroborating the results by Frenklach et al. Much later, Sankaran et al produced nano-diamonds using a dc atmospheric pressure flow-through micro-discharge plasma [22]. Synthesis of diamond nanocrystals in CCRF flow-through reactors remains elusive. Given the scarcity of characterization results of the plasmas that successfully produced nano-diamonds, the conditions required for nanocrystals of sp³-bonded carbon (i.e. nano-diamond) synthesis are not well known.

or sp^2 moieties of carbon, but never diamond itself.

At face value, this synthesis route to diamond nanocrystals appears obvious, when compared to that of silicon

synthesized in SiH₄/Ar plasmas, then simple switching to CH₄/Ar plasma would be expected to produce diamond cubic diamond nanocrystals. Such a switching was successfully implemented in CVD reactors at the Argonne National Lab where ultra-nano-crystalline-diamond (UNCD) was patented and trademarked [23]. In this work, we study this trivial switching in a moderate pressure flow-through CCRF reactor and find that carbon allotropy plays the critical role in engineering plasma and gas phase conditions to successful

diamond nanocrystal synthesis by LTP flow-through reactors.

2. Experiment

2.1. Reactor setup and sample characterization

The syntheses were carried out in a flow-through tubular reactor. A schematic of the reactor is shown in figure 1. The gases used for the synthesis were argon (or hydrogen) and methane, where methane was the carbon precursor for the reaction. The reactor consisted of a 1.27cm outer diameter quartz cylindrical tube of length 23.5cm to which the gas mixture of 100 standard cubic centimeters per minute (sccm) of argon (or hydrogen) and 2sccm of methane flowed via mass flow meters (Alicat Inc.). The total pressure measured upstream of the reaction region was between 4 and 4.2Torr. RF power of 200W at 13.56MHz from the power supply (AG0313, T&C Power Conversion) was delivered to the reactor via a copper ring electrode placed around the tube, with a ground electrode placed 3.5cm downstream of the powered electrode. An impedance matching network (MFJ 989D) was used in addition to the power supply to minimize the reflected power.

Nanomaterials were collected on stainless steel meshes or Si coupons placed downstream of the reactor. Samples were characterized using scanning electron microscopy (SEM) on a Verios 460XHR instrument , UV (325nm) Raman spectroscopy with Horiba LabRAM ARAMIS Raman instrument and grazing incidence x-ray diffraction (GIXRD) on a high resolution Rigaku SmartLab instrument with Cu K α source of wavelength 1.54Å.

2.2. Laser induced fluorescence (LIF)

LIF was used to measure the absolute densities of carbon dimer C_2 as one of the suspected pre-cursors for the synthesis of carbon nanomaterials generated from the plasma-induced reactions inside the reactor [24–26]. The LIF approach is a versatile tool for the absolute density measurement of atoms and molecules, including C_2 [27]. An Nd: YAG+OPO tunable laser system [28, 29] was used to generate the laser pulse at

fluorescence from the corresponding excitation was detected around 470nm. The excitation beam was generated by a Nd: YAG laser producing nanosecond duration laser pulses with

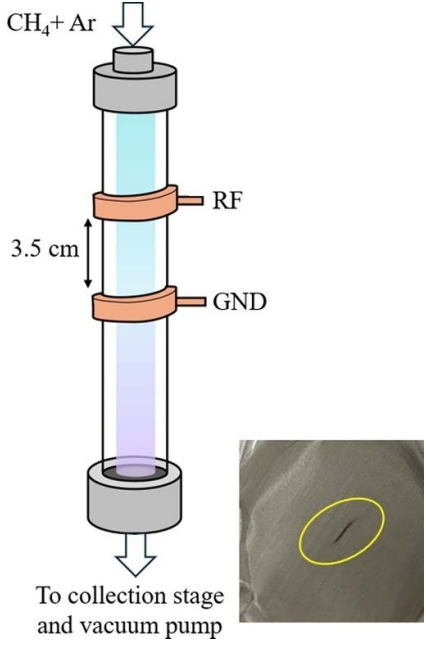


Figure 1. Schematic of the reactor with the picture of carbon nanoparticle deposition on stainless steel mesh (orifice-shaped deposition area marked by the yellow oval).

a frequency of 20Hz. The laser beam was shaped with a cylindrical lens into a laser sheath with a height of 4.2mm and width of $754\mu m$.

The laser energy was limited to $650\mu J$ per pulse. The beam passed through the cylindrical tube from one end to the other and was terminated with the help of a beam dump placed at the other side of the reactor (see LIF schematic in appendix A). The fluorescence signal is observed in a direction normal to the incoming excitation beam. A mechanical slit was situated on the detection axis, with its position and width adjusted to eliminate reflections from the sides of the tube. The detector (iCCD camera PiMAX4, Princeton Instruments, Gen III HBf intensifier) was used with a spectral filter (470nm, FWHM 10nm). The camera gate and the laser pulse were synchronized with the help of a pulse delay generator (BNC 575-4 C).

The determination of the absolute C2 molecular density from the LIF signal followed the protocol developed by Luque et al [30]. The instrumental calibration has been done by Rayleigh scattering, with the procedure described in detail in [28, 29].

2.3. Optical emission spectroscopy (OES)

Broadband OES was performed using Ocean Optics HR2000+ spectrometer for preliminary detection of various species present in the plasma. For the measurement of gas temperature,

438.8nm, to excite the (2,0) swan band transitions, and the high-resolution OES (HROES) was performed using (HRS SpectraPro 750 monochromator coupled with PiMAX4 iCCD camera) to detect CH(A-X) and C₂ emissions. In the HROES setup the entire length of the discharge tube was imaged (with demagnification) on the spectrometer slit (14 mm), so that the obtained spectra contained spatially resolved emission from all the investigated locations along the vertical axis of the iCCD screen, while the horizontal axis corresponded to the dispersion axis. A similar approach was utilized in earlier work on plasma characterization [31].

3. Results

Figure 2(a) shows the SEM image of the synthesized nanomaterial exhibiting agglomerated carbon colonies indicating its amorphous nature. The Raman spectrum from figure 2(b) shows the presence of D band around 1400cm⁻¹ and G band around 1590cm⁻¹. Ferrari and Robertson [32] demonstrated that these peak positions, when obtained using 325nm of excitation wavelength, corresponded to amorphous carbon (aC) that features sp^2 hybridization. The absence of 1332cm⁻¹ peak indicates the lack of any sp³ bonded carbon in the sample which was further confirmed from the XRD pattern (figure 2(c)) of the carbon nanoparticles depicting poor sp^2 phase crystallization with a broad peak around 23° for the graphite (002) plane and a second peak around 43.5° for the graphite (100) plane.

These characterization findings raise the question of why crystalline carbon allotropes like graphite, diamond, or lonsdaleite were not created within the reactor parameters studied here. With Si or other materials, the primary variable responsible for crystallization is the temperature of the growing nanomaterial environment (as realized via the delivered power to the reactor), [4, 33–35] and so it is important to get an estimate of the gas temperature inside the reactor along with the reactive species responsible for the formation of the obtained amorphous sp^2 carbon.

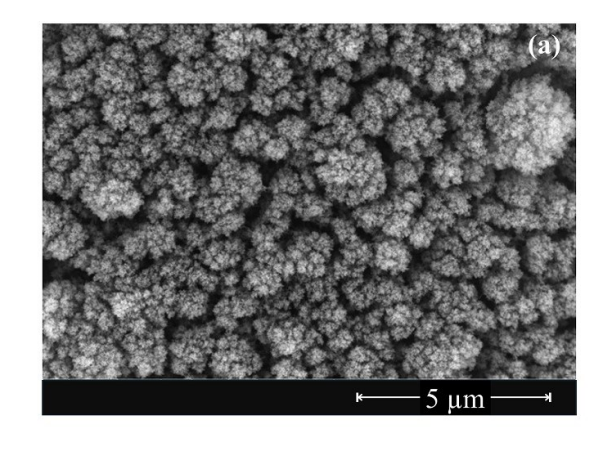
To identify the reactive species present in our reactor, we carried out a preliminary broadband OES, which revealed the presence of C2, CH, H, and Ar lines. The OES spectrum for the Ar/CH₄ plasma is shown in figure 3.

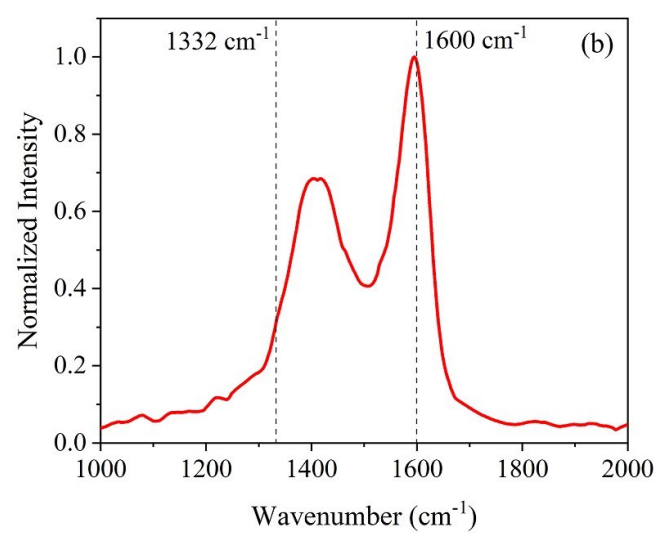
Since C_2 is attributed to play a major role in sp^2 carbon formation [36], LIF was performed using the swan band transitions in C₂ to quantify its number density in our reactor. The LIF signal S_F is related to the total number density n_0 (m⁻³) of the target species by the following equation: [30]

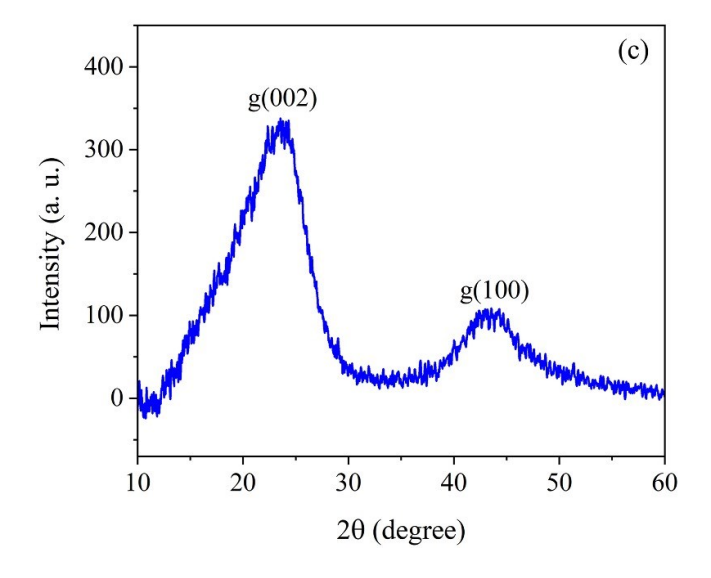
$$\underline{B} \qquad \underline{\Gamma \tau_{\text{eff}}} \left(\Omega \underline{V} \right)$$

$$SF = nofb \quad EL \qquad Ffl \qquad \varepsilon \eta \qquad (1)$$

where $f_b = 0.00655$ is the Boltzmann factor calculated following the method stated by Luque et al [37] using the







rotational and vibrational temperature of 825K and 2827K, respectively corresponding to the C₂ emission spectrum (discussed later in this section) from the following relation:

$$f_b = \frac{\exp\left(\frac{-E_{\text{vib}}}{kT_{\text{vib}}}\right)(2J+1)\exp\left(\frac{-E_{\text{rot}}}{kT_{\text{rot}}}\right)}{(2J+1)\exp\left(\frac{-E_{\text{rot}}}{kT_{\text{rot}}}\right)}$$

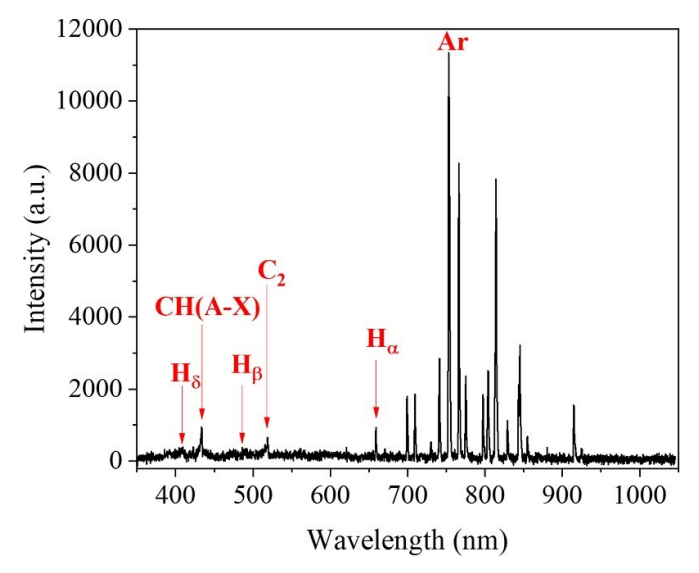


Figure3. Low-resolutionOESspectrumshowingthemain plasma-activatedspeciesintheAr/CH 4 plasma.

wavenumberand $w_e x_e = 11.67 \,\mathrm{cm}^{-1}$ istheanharmonicconstant. Taking into account the vibrational dependence of the rotational constant, b is further expressed as $b = b_e - \alpha (v + \frac{1}{2})$, [39] where $\alpha = 0.1661 \,\mathrm{cm}^{-1}$ is the vibration-rotation interaction constant and $b_e = 1.6324 \,\mathrm{cm}^{-1}$ is the rotational constant of the equilibrium state. All the constants used in the calculations have been taken from [40].

 $B = 2.5 \times 10^9 \,\mathrm{m^2 J^{-1} s^{-1}}$ is the absorption coefficient for laserexcitedrotationaltransitionasgivenin[$10^8 \,\mathrm{ms}^{-1}$ isthespeedoflight; $E_{\rm L} = 650 \times 10^{-6}$ Jisthelaser energy; Γ = 1.75 isthelineshapeoverlapintegralobtained 41]; $\Delta v = 504 \,\mathrm{m}^{-1}$ isthelaser usingtheprocessstatedin[bandwidth; $\tau_{\rm eff}/\tau_0$ isthefluorescencequantumyield, where $\tau_{\rm eff} = 79.4$ nsistheeffectivelifetimeshortened by quenching calculatedfromthetime-resolved exponential decay of the LIF signalusing [30] and $\tau_0 = 100$ nsistheradiativelifetimevalue corresponding to C_2 as given in [30]. $F_{fl} = 1$ is the fraction of lightemitted by the pumped transition in the collected spectralregion. Ω is the solid angle of the laser-probed volume ε is the transmission efficiency of the optics, η isthephotoelectricefficiencyofthephotomultiplier, and A_L isthelaser cross-sectionarea.

Theterm $(\frac{\Omega}{4\pi} \varepsilon \eta \frac{V}{A_L})$ is determined by the calibration measurements of Rayleighscattering of air. The Rayleigh signal of the incident light collected at a normal angle is given by the following relation: [30]

$$S_{R} = N \frac{E_{L}}{\Omega \varepsilon \eta} \frac{\partial \sigma}{\Omega \varepsilon \eta} V$$

$$Q_{Vib}Q_{rot}Q_{elec}$$
(3)

where $E_{\rm vib}$ and $E_{\rm rot}$ are the vibrational and rotational energies, (2*J*+1) is the rotational degeneracy. $Q_{\rm vib}$, $Q_{\rm rot}$, and $Q_{\rm elec}$ **Figure 2.** (a) SEM morphology, (b) UV Raman spectrum and (c) XRD pattern of the material synthesized using the CCRF reactor.

are the vibrational, rotational and electronic partition high in the traditional sense. Outside wall temperature where b is the effective rotational constant and J is the temperature) to the wall (low temperature). rotational energy level; $E_{\text{vib}} = w_e(v + \frac{1}{2}) - w_e x_e(v + \frac{1}{2})^2$, [39] where v is the quantum energy level, $w_e = 1641.35 \text{cm}^{-1}$ is the vibrational

$$\frac{}{hcv}\frac{}{\partial\Omega}$$
 $A_{\rm I}$

where N = p/kT is the gas number density, pressure p=1atm or 101325Pa, $k = 1.38 \times 10^{-23}$ JK⁻¹ is the Boltzmann constant, and gas temperature T = 293K; $h = 6.626 \times 10^{-34}$ Js is the Planck's constant; $v = (438 \times 10^{-9})^{-1}$ m⁻¹ is the wavenumber of the scattered photon; $\frac{\partial \sigma}{\partial \Omega} = 1.418 \times 10^{-31} \text{ m}^2\text{sr}^{-1}$ is the Rayleigh cross section corresponding to the polarizability of air= 1.8×10⁻³⁰ m³ and depolarization ratio of air=0.028 calculated using [42]. The slope of the plot S_R vs $(E_L \times p)$, obtained by varying $E_{\rm L}$ from 1.7 to

17mJ at atmospheric pressure, is used to calculate the term This at authospheric pressure, is used to calculate the term $\binom{\Omega}{4\pi} \varepsilon \eta_{-} A^{\underline{V}_L}$) which is plugged in equation (1) to give the absolute number density of $C_2 \sim 10^{18} \, \mathrm{m}^{-3}$. This concentration of C_2 in the highly collisional plasma is sufficient for the formation of sp^2 phase carbon nanomaterial [30, 43].

To estimate the gas temperature in the reactor during synthesis, HROES was used to measure the C_2 emission spectrum around 516nm and was fitted in Specair software

spectrum around 516nm and was fitted in Specair software [44] which calculates the molecular spectrum of a species for a given set of rotational and vibrational temperatures. A theoretical spectrum was thus generated that best fits the experimentally obtained spectrum giving a rotational temperature of 825K and a vibrational temperature of 2827K (see figure 4).

To extrapolate the reactor gas temperature from this measurement requires the assumption that there is thermal equilibrium among the heavy species in the plasma (though the electrons have much higher energies), and that the rotational temperature is similar to the gas temperature [45]. From these assumptions, the C2 spectrum indicated the gas temperature of ~800-900K in the reactor. This temperature is too low to induce crystallization via gas heating because crystallization temperatures of graphite or diamond exceed 1300 K. Furthermore, in a previous study, the authors reported that higher temperature promotes graphitization in CVD systems [46].

The gas temperature finding of ~800-900K deserves closer consideration. In capacitively-coupled flow-through reactors, gas temperature has been said to remain close to room temperature, exceeded only by a couple of hundred Kelvin [47]. In the present study, the variable in question is apparently

functions, respectively. The energies of the rotational and measured by an attached thermocouple indicates that there vibration states are calculated from $E_{rot}(J) = bJ(J+1)$, [38] must be a temperature gradient from the reaction zone (high

4. Discussion

The most plausible hypothesis that could explain selfconsistently the extreme thermal gradient in the reactor (~500K between centerline and wall) and, otherwise the overall amorphous sp^2 product output is the presence of a hot filamentary region (in other words, plasma constriction) in the centerline of the reactor. If this were true, then RF power would be absorbed by the constricted plasma, thereby immensely increasing the power density and hence heating it to the condition of a hot wire. The rest of the reactor where gas flows at a given velocity would then receive additional heating through thermal conductivity and diffusivity.

To prove this hypothesis, first, a separate experiment in a linch tube (same reactor parameters as described in

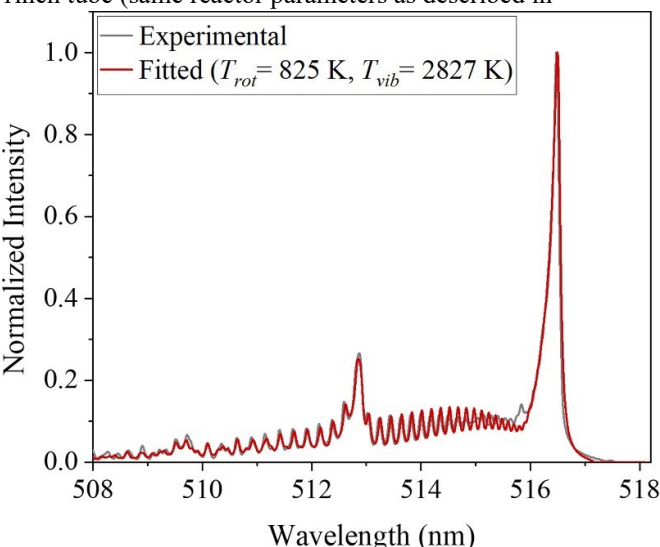


Figure 4. Experimental (from HROES) vs fitted spectrum for C₂ used for gas temperature calculation.

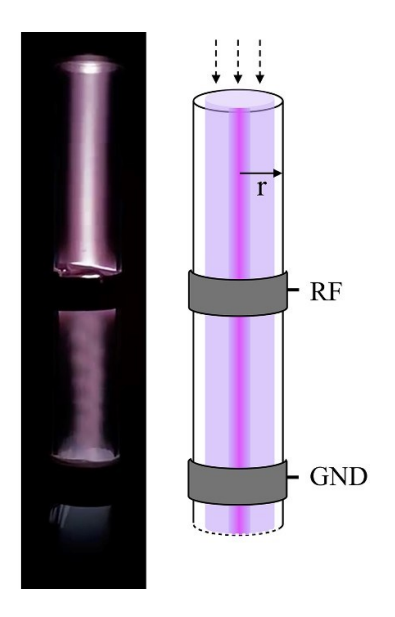
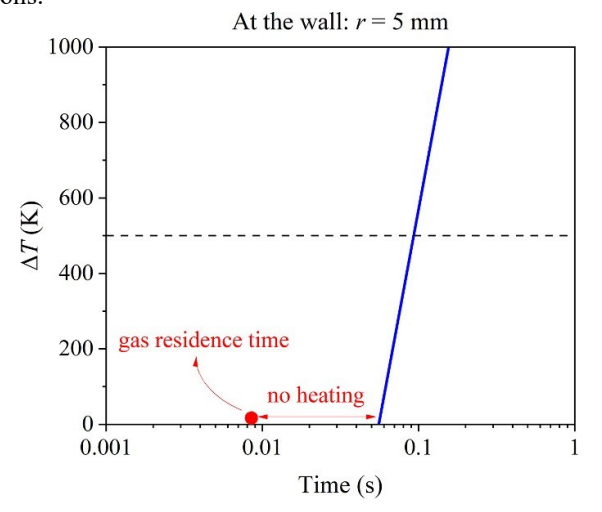


Figure 5. (Left) Photograph and (right) demonstration and model of the hot filament.

section 2.1) was conducted to exaggerate the spatial dimension and better visualize any potential constricted region. The result is shown in figure 5(left), in which a bright straight columnar structure in the middle of the reactor can be seen. This observation is then converted into a model representation shown in figure 5(right). To connect the hot wire observation to the measurement results, the applied power portion absorbed by the plasma (i.e. electrons) and not the sheath must be determined. A formula derived by Godyak *et al* [48] was used. Equation (4) represents the ratio between the power absorbed by the ions in the sheath and the power absorbed by electrons:





Here, $v_s = \sqrt{eqT_{M^e}}$ is the ion Bohm velocity at the plasmasheath edge, with e being the electron charge, q being the state of charge of ions, and T_e being the electron temperature. Since CH₄ is a minor fraction of the feedstock mixture dominated by the argon flow, it is plausible to assume that the gas properties are largely defined by those of argon. Hence, M can be approximated as the argon atom mass. With $T_e = 2eV$ [49],

 $M = 6.6 \times 10^{-26}$ kg, v_s becomes 2.2×10^3 ms⁻¹. $\omega_e = \sqrt{m_e^{e_2}n_e^{e_0}}$ is the plasma frequency with n_e being electron concentration m_e being the electron mass and ϵ_0 being the vacuum permittivity. With $n_e = 10^{17}$ m⁻³, [49, 50] $m_e = 9.1 \times 10^{-31}$ kg, and $\epsilon_0 = 8.85 \times 10^{-12}$ F m⁻¹, ω_e becomes 1.78×10^{10} s⁻¹. v_{en} is the electron-neutral collision frequency. Using a scaling for argon from Raizer [51] as $v_{en} = p \times 5.3 \times 10^9$ Torr \times s⁻¹Torr⁻¹, v_{en} becomes 2.12×10^{10} s⁻¹ for p=4 Torr. With d = L/2 = 1.75cm, where L is the distance between the electrodes as shown in figure 1, and the source frequency $\omega = 13.56$ MHz, we finally find $P_i/P_e = 15.4$. Next, the input power P_{in} can be written as $P_{in} = P_i + P_e = P_e(1 + p_e^{D_e}L)$. Then, a new relation for the finalized P_e can be written:

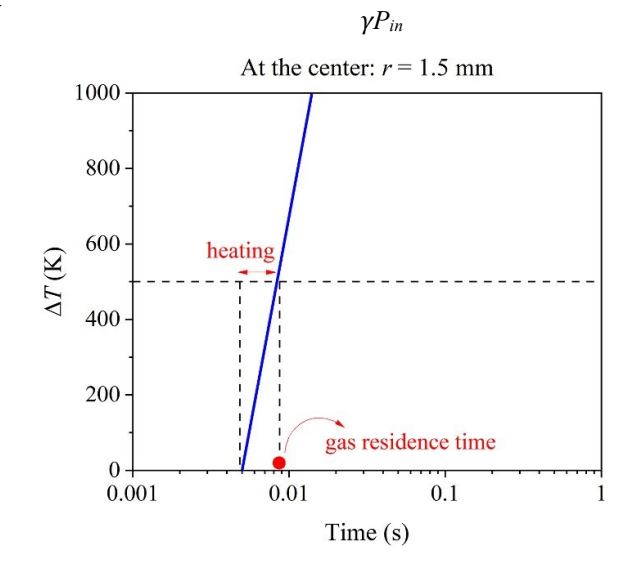


Figure 6. The temporal dependence of the relative temperature increase according to equation (6) with the specified parameters. These calculations do not include the heating taking place at the metal electrodes.

$$P = \frac{1}{1 - p_0}$$

where γ is the matchbox efficiency. With assumed $\gamma = 0.7$, the nominal input power of 200W results in 8.5W given to the electrons.

Because the ionization degree of the studied discharge was low, it is then plausible to treat the reactor medium as a neutral gas. Further on, assuming that the gas properties are largely defined by those of argon, the plasma is approximated as a thin hot wire source. Mathematically, the hot wire model, shown in figure 5(right), can be expressed by the gas heating ΔT [52] as:

$$\Delta T(r, t) = \frac{P_e/L}{4\pi \lambda} ln \left(\frac{4\alpha t}{r^2 C}\right)$$
 (6)

where $C = e^{0.577} = 1.781$, α is the thermal diffusivity, λ is the thermal conductivity, and P_e/L is the linear power density. Equation (6) quantifies the gas heating ΔT relative to the room temperature of 300K at different coordinates r, from the reactor center to the wall, as a function of time t. This mathematical model is applicable for a collisional plasma, i.e. the condition of r > [mean free path] must be satisfied. From the calculations detailed in appendix B, equation (6) is applicable at any $r > 0.23 \, \text{mm}$.

Since the atom-atom mean free path is much smaller than the radius of the tube, we use the thermophysical data presented in [53] to find $\alpha = 20 \times 10^{-5} \, \text{m}^2 \text{s}^{-1}$ and $\lambda = 0.02 \, \text{WmK}^{-1}$. From equation (6), the plot presented in figure 6(left) shows a striking result: to enhance a measurable temperature increase on the wall, the gas flowing through the reactor has to spend at least $\sim 0.06 \, \text{s}$. At the same time, the residence time of the gas τ is only 0.0087s, calculated as follows:

$$\pi d^2 L 60$$

$$\tau = \underline{\qquad} \underline{\qquad} p_{\underline{a}} 1 \qquad (7) q_p$$

where q is the flow rate in sccm, p_a is the atmospheric pressure of 760Torr and p is the operating reactor pressure, and 60/1 is the minute-to-second conversion. With p=4Torr, equation (7) yields the noted residence time of 0.0087s and a gas flow velocity of $4.03 \,\mathrm{ms}^{-1}$. On the other hand, at the center of the tube, as shown in figure 6(right), this residence time is enough to increase the gas temperature by $\sim 500 \,\mathrm{K}$ above room temperature.

Hence, from the model results it is seen that the main body (right outside the hot filament) of the discharge is cold. These results now can be used to explain the synthetis results. Once methyl radical is generated from a methane molecule, the activation energy for the initial step ${}^{\bullet}CH_3 + {}^{\bullet}CH_3 \rightarrow {}^{\bullet}C_2H_6$ to eventually form an adamantane molecule is high, close

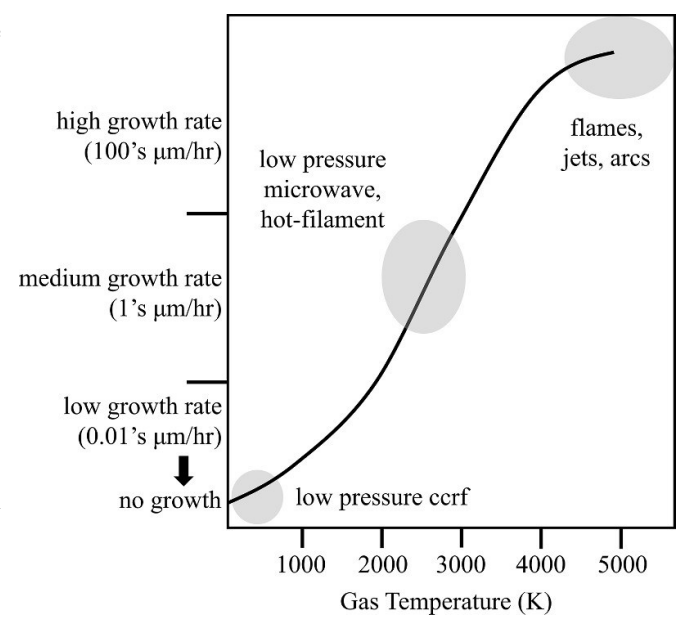
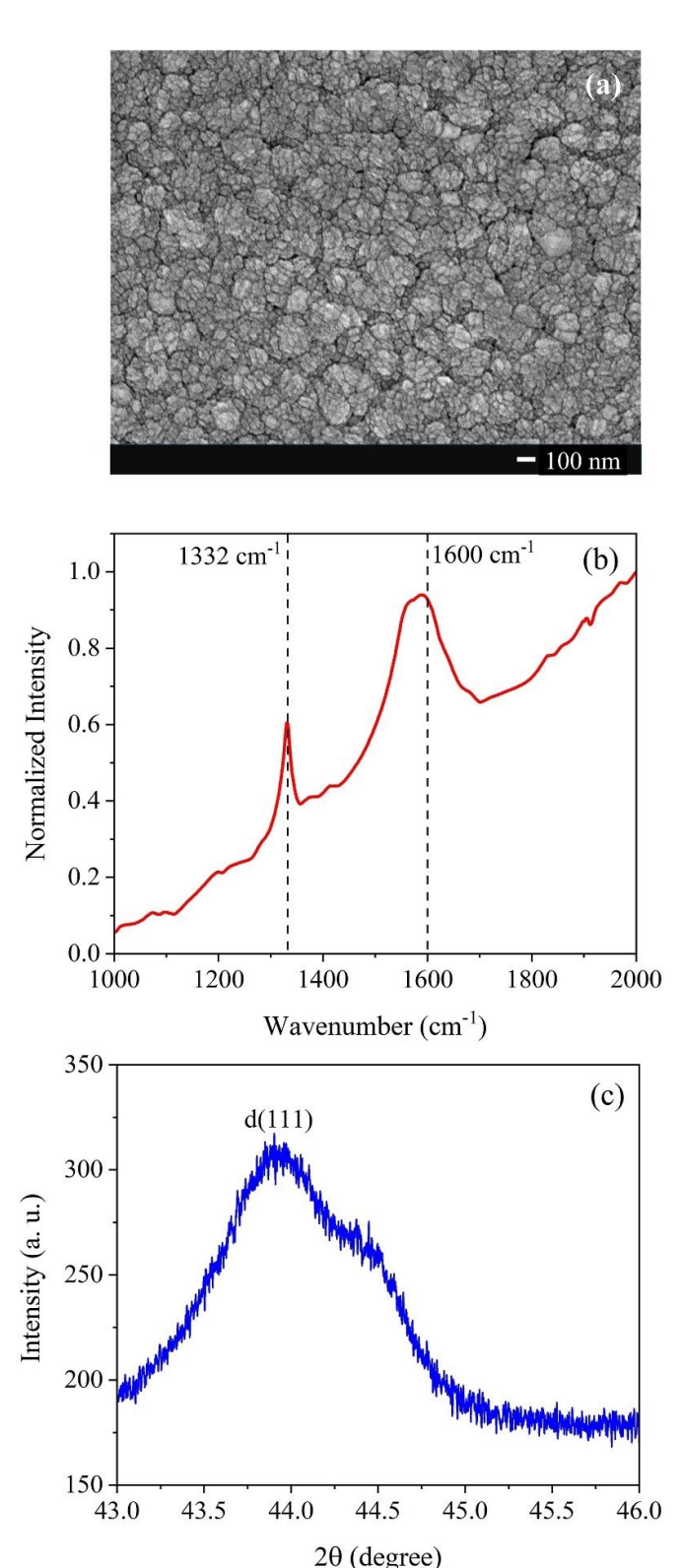


Figure 7. Growth rate versus gas temperature comparison chart of the main diamond synthesis techniques [59] with the addition of the low pressure RF plasma where no diamond growth was achieved.

or above 13kJmol^{-1} with a reaction rate $\lesssim 10^{-11} \, \text{cm}^3 \text{s}^{-1}$ [54]. To counter this limited kinetics, a higher gas temperature is required. At the same time, sp^2 graphitic reactions are expected to be virtually barrierless [55] explaining immense product formation in cold Ar/CH₄ discharge. The cold gas medium does not allow sp^2 to crystallize leaving it in an amorphous state. While the same process should be happening in H₂/CH₄, sp^2 phase is immediately etched by atomic hydrogen with net zero product effect. The nonexistence of Si allotropy is the main reason of successful and welldeveloped Si syntheses with capacitively coupled RF continuous flow-through reactors, where *SiH₃ + *SiH₃ reactions are barrierless [56].

The limiting nature of methyl radical chemistry in the gas phase or on the substrate [57] explains well why CVD reactors have to operate at high gas and substrate temperatures. From this, various diamond reactors can be compared as shown in figure 7. Diamond growth starts at gas temperatures above 1000K. In the early 1980's, small tubular DC flame, jet or arc reactors were successfully developed and used for diamond synthesis at high production rates [58]. These designs were obviously successful because their operating gas temperatures are near 5000K allowing for fast diamond kinetics. At the same time, such designs were quickly ruled out due to scalability issues and cavity microwave reactors became the industrial workhorses for single crystal diamond wafer productions.



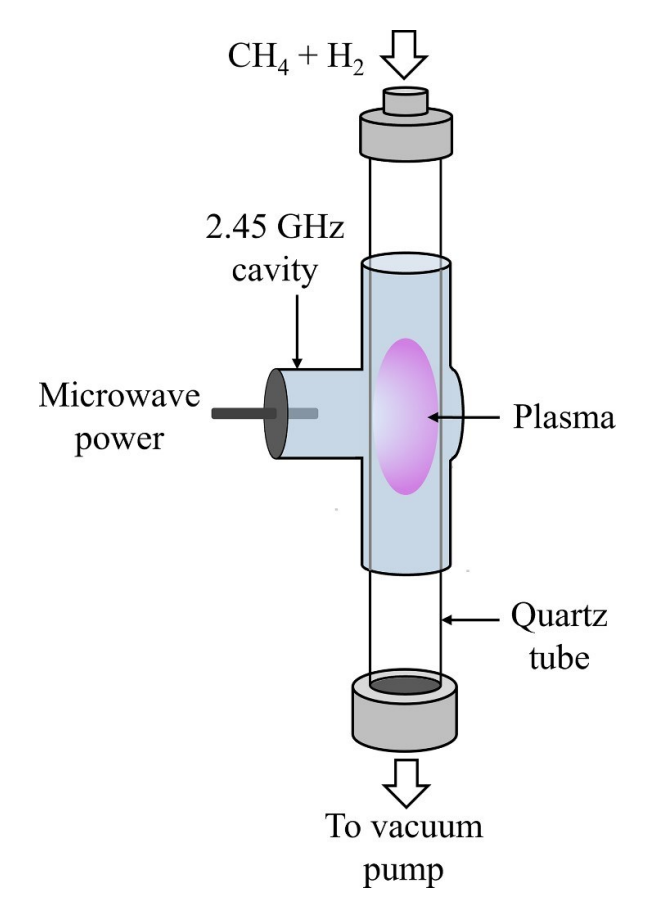


Figure 8. Schematic of the flow-through microwave reactor.

In the new era of 3D additive manufacturing, reactor compactness is a plus, and flames, jets and arcs could be reconsidered for nanodiamond production. Talking about flow-through reactors, a number of new reactor strategies can be proposed. For CCRF, ambient pressure reactors of very small diameters could be beneficial for nanodiamond production. The plasma constriction (aka hot filament) is an unstable effect, therefore the easiest way to seize the hot gas filament is to induce it in a narrow capillary. High pressure increases RF power to electron coupling because, according to equation (4), P_i/P_e ratio decreases. For larger reactor volumes, inductively coupled flow-through systems could be useful such that gas heating is optimized for best diamond chemistry/kinetics. Third option could be using microwave flow through reactors where gas temperature can be manipulated by the same pressure-power product but in much wider ranges over a wider range of reactor volumes thanks to more efficient microwave to plasma power coupling.

To test this hypothesis, a proof-of-concept flow-through microwave CVD reactor was developed, the schematic of whichisshowninfigure8. Thereactorconsists of aquartz tube Figure 9. (a) SEM morphology, (b) UV Raman spectrum, and (c) XRD pattern of the material synthesized using the microwave reactor.

placed inside a compact cylindrical 2.45GHz cavity, thereby replacing the RF ring electrodes. In preliminary experiments,

precursor gases, H₂ and CH₄, were flown through the tube to **Acknowledgment** generate a stable plasma discharge. The reactor was operated under a similar pressure-power product regime as that of the CCRF reactor and samples were collected on a Si coupon placed in the reactor tube away from plasma. The morphology of the collected sample was typical to that of nanodiamond [46] as seen from the SEM image in figure 9(a), which consists mainly of sp^3 bonded carbon along with some amount of sp^2 bonding. The Raman spectrum in figure 9(b) shows the presence of G peak around 1590cm⁻¹ corresponding to sp² bonded carbon and a strong 1332 cm⁻¹ peak, a key marker attributed to sp3 diamond phase. The XRD pattern clearly reveals the presence of diamond (111) peak [46] at 43.9° as shown in figure 9(c). From modeling [60], it was found that the microwave reactor had extremely efficient cavity-toplasma power transfer leading to a gas temperature of ~2000K. These results substantiate the hypothesis that gas temperature is a critical parameter in the synthesis of carbon nanomaterials via flow-through plasmas.

5. Conclusion

A flow-through CCRF reactor utilizing Ar/CH₄ mixture was attempted to synthesize diamond nanocrystals. For standard conditions 4Torr and 200W, typical for diamond-cubic Si and Ge nanocrystal syntheses, final product material analyses revealed that only a sp^2 graphitic nanomaterial could be obtained, and with a fraction of sp³ diamond nanocrystals (if any at all) that could not be registered experimentally. Using high-resolution LIF and OES diagnostics of the reactor, it was shown that power density and hence gas heating is concentrated in the narrow 1.5mm on the axial region of the reactor, while the remainder of the plasma volume contains cold gas. This promotes the formation of thermodynamically favorable graphitic allotrope, although some small amount of sp^3 hybridization in the material cannot be ruled out. If the same reactor was switched to operate with H₂/CH₄ mixture (traditionally used for diamond synthesis), no product was detected to form because atomic hydrogen actively must have etched the sp^2 hybridized nanomaterial, thereby leading to a net zero synthesis effect.

successfully synthesize sp³ hybridized carbon from a H₂/CH₄ number density calculation of C₂. feedstock owing to higher gas temperature. These results put into context the legacy polycrystalline diamond synthetic routes, and outline practical strategies that could allow for future diamond nanocrystal feedstock production using flowthrough low-temperature plasma reactors for bottom up additive manufacturing.

Data availability statement

All data that support the findings of this study are included within the article (and any supplementary files).

This work was supported by the U.S. Department of Energy, Office of Science, Office of Fusion Energy Sciences, Award No. DE-SC0023211, and National Science Foundation, Division of Chemical, Bioengineering, Environmental and Transport Systems, Award No. 2333452. Work at Princeton Collaborative Low Temperature Plasma Research Facility (PCRF) was supported by the U.S. Department of Energy under Contract No. DE-AC02-09CH11466.

Conflict of Interest

The authors have no conflicts to disclose.

Appendix A. Setup for plasma diagnostics

The schematics of the diagnostic setup is shown in figure 10. This was the same setup used in [28, 29] where details of each componentandthesettingsusedtooperatethemaredescribed. The tunable laser system consists of a Nd YAG laser pumping an optical parametric oscillator (OPO). The laser beam out of the OPO was shaped with a cylindrical lens. The beam was then guided to the plasma, where the laser photons interact with the plasma species creating emissions that were then collected as LIF and OES signals in direction normal to the laser propagation axis. The HROES signal was imaged at the entrance slit of the monochromator to which an iCCD camera was coupled. The LIF signal detector was an iCCD camera equipped with a spectral filter and an objective lens.

The calibration for LIF measurements was done by Rayleigh scattering performed with the same detection setup as for LIF according to the procedure followed by Yatom et al [29]. Signals from Rayleigh scattering of air were recorded by varyingthelaserpulseenergyfrom 1.7 to 17 mJatatmospheric pressure. The energy of the laser pulse was varied using a series of optical density filters from 0.2 to 1. The resultant plot of S_R vs $(E_L \times p)$ is shown in figure 11 obtaining a slope of A flow-through microwave reactor was demonstrated to 219860J⁻¹Pa⁻¹ which is used in equation (1) for the absolute

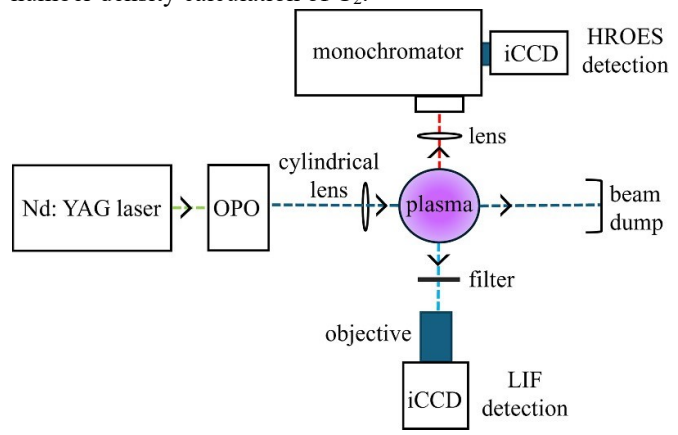


Figure 10. Schematic of the setup used for LIF and HROES measurements.

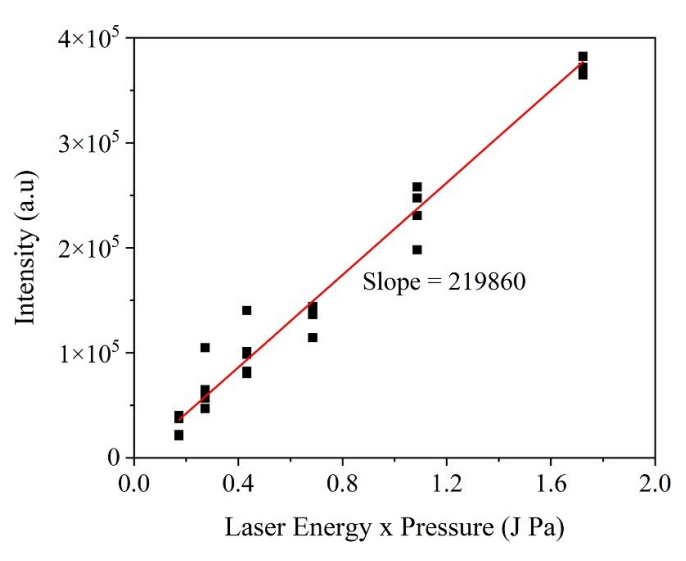


Figure 11. The plot of S_R vs $(E_L \times p)$ from Rayleigh scattering.

Appendix B. Applicability of equation (6)

Equation (6) gives an upper limit boundary for the maximum attainable temperature for a given distance r from the center of the tube, assuming no radiation losses. Equation (6) is applicable to collisional systems, i.e. as long as r is larger than the mean free path of Ar. Mean free path can be calculated as follows:

$$l = \sqrt{k^{\rm B}} \frac{T}{\sqrt{2\pi d_{2\rm Ar}p}}$$

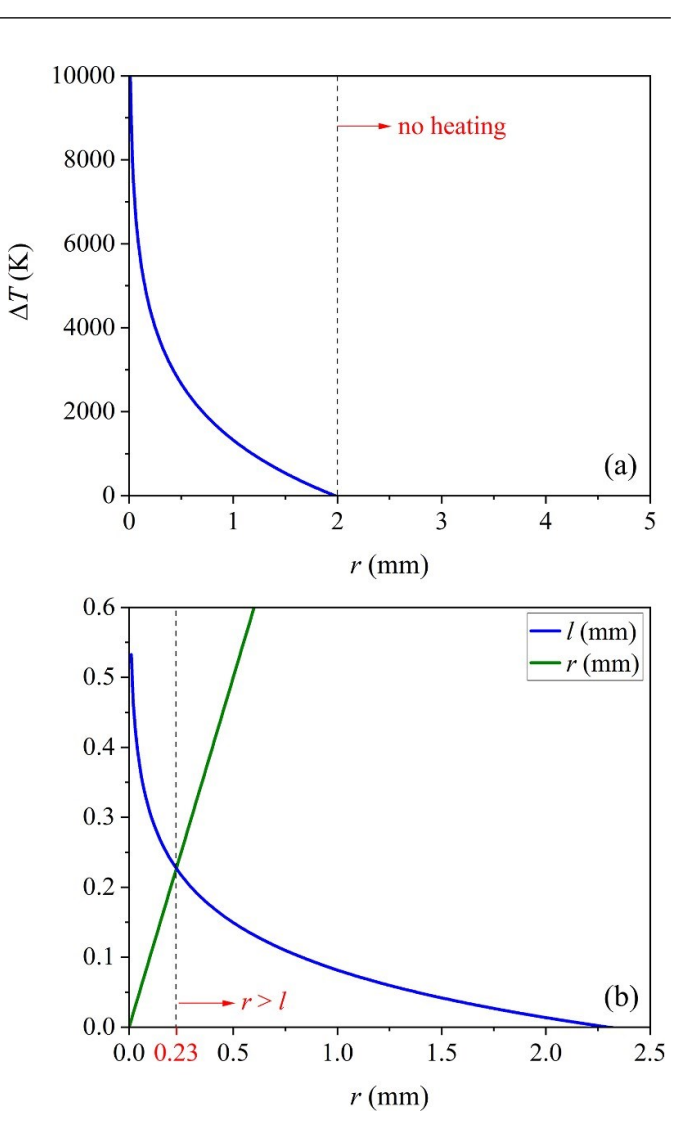


Figure 12. (a) ΔT corresponding to the gas residence time of 0.0087s, and (b) the corresponding mean free path as a function of r.

where $k_{\rm B} = 1.38 \times 10^{-23} \, {\rm JK^{-1}}$, $T = \Delta T(r,t) + 293 \, {\rm K}$, $d_{\rm Ar} = 3.4 \times 10^{-10} \, {\rm m}$ is the kinetic diameter of Ar, and $p = 4 \times 133.32 \, {\rm Pa}$. The residence time of gases in the CCRF reactor presented here is 0.0087s. During this time, gas heating ΔT as a function of r for the 5mm radius of the reactor chamber can be plotted as shown in figure 12(a). Using this $\Delta T(r)$, mean free path as a function of r can be plotted as in figure 12(b) which sets the boundary condition for the applicability of equation (6) as $r > 0.23 \, {\rm mm}$. According to this model, the maximum attainable temperature at $r = 0.23 \, {\rm mm}$ is 4000K.

ORCID iDs

Tanvi Nikhar □ https://orcid.org/0000-0001-8363-5076 Sankhadeep Basu □ https://orcid.org/0000-0001-5220-2614 Yevgeny Raitses □ https://orcid.org/0000-0002-9382-9963

Sergey V Baryshev □ https://orcid.org/0000-0002-91265658 **References**

- [1] Graves D, Labelle C and Kushner M 2023 Report on Science Challenges and Research Opportunities for Plasma Applications in Microelectronics (Department of Energy Office of Science, Fusion Energy Sciences) (available at: https://science.osti.gov/-/media/fes/pdf/2023/DOE_FES_PlasmaScience_Semiconductors_Final.pdf)
- [2] Adamovich M et al 2017 J. Phys. D: Appl. Phys 50 323001
- [3] Kortshagen U R, Sankaran R M, Pereira R N, Girshick S L, Wu J J and Aydil E S 2016 *Chem. Rev.* 116 11061
- [4] Anthony R and Kortshagen U 2009 Phys. Rev. B 80 115407
- [5] Kortshagen U 2016 Plasma Chem. Plasma Process. 36 73
- [6] Mangolini L and Kortshagen U 2007 Adv. Mater. 19 2513–9
 [7] Woodard A, Xu L, Barragan A A, Nava G, Wong B M and Mangolini L 2018 Plasma Process. Polym. 15 1700104
- [8] Exarhos S, Alvarez-Barragan A, Aytan E, Balandin A A and Mangolini L 2018 ACS Energy Lett. 3 2349 [9] Thimsen E, Kortshagen U R and Aydil E S 2015 J. Phys. D: Appl. Phys. 48 314004
- [10] Uner N B, Niedzwiedzki D M and Thimsen E 2019 J. Phys. Chem. C 123 30613
- [11] Izadi A and Anthony R J 2019 Plasma Process. Polym. 16 e1800212
- [12] Mandal R, O'Shea K and Anthony R 2018 J. Vac. Sci. Technol. A 36 051303
- [13] Ho A, Mandal R, Lunt R R and Anthony R J 2021 ACS Appl. Nano Mater. 4 5624
- [14] Dsouza S D, Buerkle M, Alessi B, Brunet P, Morelli A, Payam A F, Maguire P, Mariotti D and Svrcek V 2023 Nanotechnology 34 505601
- [15] Askari S, Macias-Montero M, Velusamy T, Maguire P, Svrcek V and Mariotti D 2015 J. Phys. D: Appl. Phys. 48 314002
- [16] Nozaki T, Sasaki K, Ogino T, Asahi D and Okazaki K 2007 J. Therm. Sci. Technol. 2 192
- [17] Mangolini L, Thimsen E and Kortshagen U 2005 Nano Lett. 5 655
- [18] Pi X and Kortshagen U 2009 Nanotechnology 20 295602 [19] Gresback R, Holman Z and Kortshagen U 2007 Appl. Phys. Lett. 91 093119
- [20] Deryagin B V and Fedoseev D V 1979 Bull. Acad. Sci. USSR Div. Chem. Sci. 28 1106
- [21] Frenklach M, Kematick R, Huang D, Howard W, Spear K, Phelps A W and Koba R 1989 J. Appl. Phys. 66 395
- [22] Kumar A, Ann Lin P, Xue A, Hao B, Khin Yap Y and Sankaran R M 2013 *Nat. Commun.* 4 2618
- [23] Auciello O 2022 Funct. Diam. 2 1
- [24] Yatom S, Khrabry A, Mitrani J, Khodak A, Kaganovich I, Vekselman V, Stratton B and Raitses Y 2018 MRS Commun. 8 842
- [25] Yatom S, Bak J, Khrabryi A and Raitses Y 2017 Carbon 117 154
- [26] Stratton B, Gerakis A, Kaganovich I, Keidar M, Khrabry A, Mitrani J, Raitses Y, Shneider M, Vekselman V and Yatom S 2018 Plasma Sources Sci. Technol. 27 084001
- [27] Vekselman V, Khrabry A, Kaganovich I, Stratton B, Selinsky R and Raitses Y 2018 *Plasma Sources Sci. Technol.* 27 025008
- [28] Yatom S and Dobrynin D 2022 J. Phys. D: Appl. Phys. 55 485203

- [29] Yatom S, Chopra N, Kondeti S, Petrova T B, Raitses Y, Boris D R, Johnson M J and Walton S G 2023 Plasma Sources Sci. Technol. 32 115005
- [30] Luque J, Juchmann W and Jeffries J 1997 J. Appl. Phys. 82 2072
- [31] Yatom S and Raitses Y 2020 Phys. Chem. Chem. Phys. 22 20837
- [32] Ferrari A C and Robertson J 2001 Phys. Rev. B 64 075414 [33] Galli F and Kortshagen U R 2009 IEEE Trans. Plasma Sci. 38 803
- [34] Mangolini L and Kortshagen U 2009 Phys. Rev. E 79 026405
- [35] Lopez T and Mangolini L 2014 J. Vac. Sci. Technol. B 32 061802
- [36] Mahoney E J, Rodriguez B J, Mushtaq S, Truscott B S, Ashfold M N and Mankelevich Y A 2019 J. Phys. Chem. A 123 9966
- [37] Luque J, Juchmann W and Jeffries J 1997 Appl. Opt. 36 3261
- [38] Hollas J M 2004 Modern Spectroscopy 4th edn (Wiley) Ch 5, p
- [39] Hollas J M 2004 Modern Spectroscopy 4th edn (Wiley) Ch 6, p
- [40] Huber K P and Herzberg G 1979 Molecular Spectra and Molecular Structure Volume IV Constants of Diatomic Molecules (Springer) p 114
- [41] Partridge W P and Laurendeau N M 1995 Appl. Opt. 34 2645
- [42] Reichardt J, Baumgart R and McGee T J 2003 Appl. Opt. 42 4909
- [43] Kruis F E, Schoonman J and Scarlett B 1994 J. Aerosol. Sci. 25 1291
- [44] Laux C O Fletcher D, Charbonnier J-M, Sarma G S R and Magin T 2002 Radiation and nonequilibrium collisionalradiative models *Physico-Chemical Modeling of High Enthalpy* and *Plasma Flows* (von Karman Institute Lecture Series 2002-07) ed D Fletcher, J M Charbonnier, G S R Sarma and T Magin (Rhode-Saint-Genèse)
- [45] Bruggeman P J, Sadeghi N, Schram D and Linss V 2014 Plasma Sources Sci. Technol. 23 023001
- [46] Nikhar T, Rechenberg R, Becker M F and Baryshev S V 2020 J. Appl. Phys. 128 235305
- [47] Agarwal A, Rauf S and Collins K 2012 Plasma Sources Sci. Technol. 21 055012
- [48] Godyak V, Piejak R and Alexandrovich B 1991 J. Appl. Phys. 69 3455
- [49] Godyak V and Piejak R 1990 Phys. Rev. Lett. 65 996
- [50] Moravej M, Yang X, Nowling G, Chang J, Hicks R and Babayan S 2004 *J. Appl. Phys.* **96** 7011
- [51] Raizer Y P 1997 *Gas Discharge Physics* vol 2, ed J E Allen (Springer)
- [52] Assael M J, Antoniadis K D, Velliadou D and Wakeham W A 2023 Int. J. Thermophys. 44 85
- [53] Sun L and Venart J 2005 Int. J. Thermophys. 26 325
- [54] Forst W 1991 J. Phys. Chem. 95 3612
- [55] Fedoseev D, Vnukov S and Derjaguin B 1979 Carbon 17 453
- [56] Matsui Y, Yuuki A, Morita N and Tachibana K 1987 Jpn. J. Appl. Phys. 26 1575
- [57] Kang J K and Musgrave C B 2000 J. Chem. Phys. 113 7582
- [58] Haubner R 2021 *ChemTexts* 7 10
- [59] Bachmann P K, Leers D and Lydtin H 1991 Diam. Relat. Mater. 1 1
- [60] Nikhar T and Baryshev S V Microwave Capillary

Nanodiamond Reactor Patent Pending